OPEN

Merging of Kirkendall Growth and Ostwald Ripening: CuO@MnO$_2$ Core-shell Architectures for Asymmetric Supercapacitors

Ming Huang[1], Yuxin Zhang[1,2], Fei Li[1], Zhongchang Wang[3,4], Alamusi[4], Ning Hu[4], Zhiyu Wen[2] & Qing Liu[1]

[1]College of Materials Science and Engineering, Chongqing University, Chongqing 400044, China, [2]National Key Laboratory of Fundamental Science of Micro/Nano-Devices and System Technology, Chongqing University, Chongqing 400044, China, [3]WPI, Advanced Institute for Materials Research, Tohoku University, 2-1-1 Katahira, Aoba-ku, Sendai 980-8577, Japan, [4]Department of Engineering Mechanics, College of Aerospace Engineering, Chongqing University, Chongqing 400044, China.

Correspondence and requests for materials should be addressed to Y.X.Z. (zhangyuxin@cqu.edu.cn); Z.C.W. (zcwang@wpi-aimr.tohoku.ac.jp) or Q.L. (qingliu@cqu.edu.cn)

Fabricating hierarchical core-shell nanostructures is currently the subject of intensive research in the electrochemical field owing to the hopes it raises for making efficient electrodes for high-performance supercapacitors. Here, we develop a simple and cost-effective approach to prepare CuO@MnO$_2$ core-shell nanostructures without any surfactants and report their applications as electrodes for supercapacitors. An asymmetric supercapacitor with CuO@MnO$_2$ core-shell nanostructure as the positive electrode and activated microwave exfoliated graphite oxide (MEGO) as the negative electrode yields an energy density of 22.1 Wh kg^{-1} and a maximum power density of 85.6 kW kg^{-1}; the device shows a long-term cycling stability which retains 101.5% of its initial capacitance even after 10000 cycles. Such a facile strategy to fabricate the hierarchical CuO@MnO$_2$ core-shell nanostructure with significantly improved functionalities opens up a novel avenue to design electrode materials on demand for high-performance supercapacitor applications.

Supercapacitors, known as electrochemical capacitors, hold substantial promise for next-generation power devices due to their excellent properties such as high power density, fast charge and discharge rate, excellent reversibility, and long cycle life[1–4]. In general, they can be divided into two categories in light of their charge storage mechanisms: the electric double-layer capacitors (EDLCs) and the pseudo-capacitors[5–9]. To date, much effort has been devoted to the latter using transition-metal oxides including MnO$_2$[10,11], Co$_3$O$_4$[12,13], NiO[14,15], VO$_x$[16,17], and CuO[18–20] because they bear a much higher specific capacitance and energy density compared to carbon-based materials and conducting polymers. Moreover, they have a variety of oxidation states so as to allow the efficient redox charge transfer. In addition, they are of low cost.

Among the available transition-metal oxides, MnO$_2$ has attracted a great deal of attention for its role as an electrode material for supercapacitors due to its abundance, high theoretical capacity ($\sim$1370 F g^{-1}), non-toxicity, and wide operating potential range in mild electrolyte[21–25]. It is thus currently the subject of intensive research to fabricate MnO$_2$ with different morphologies and examine associated electrochemical properties. However, the key issues limiting its widespread applications rest with its low surface area and poor electronic conductivity. To overcome the issues, many techniques have been attempted, yet most of them involve the preparation of MnO$_2$-conductive matrix hybrid nanostructures through incorporating MnO$_2$ with conductive support[26–32]. Such hybrid system can show high-rate and cycling ability due to the relatively low weight fraction of its active materials. However, it has low energy density. Although this can be resolved by developing novel hybrid pseudo-capacitive systems *via* combining the metal oxides with binary metal oxide/hydroxides, the electrochemical performance of these systems remains unsatisfactory. This is due to the intricacies in fabricating well defined micro/nano-structure and also because of lack of knowledge of the synergistic effects[33,34]. To address these issues, the MnO$_2$-based nanocomposites with a range of morphologies has been developed as electrodes for supercapacitors, aimed to enhance their electrochemical function, including Co$_3$O$_4$@MnO$_2$, Fe$_2$O$_3$@MnO$_2$, ZnO@MnO$_2$, TiO$_2$@MnO$_2$, NiCo$_2$O$_4$@MnO$_2$, and Co$_3$O$_4$@Pt@MnO$_2$[33,35–40]. Taking the amount of challenges and opportunities, creating integrated smart architectures with well-defined structures, improved electroactivity, and faster ion and electron transport is timely and important.

Here, we developed a simple and cost-effective method to fabricate hierarchical CuO@MnO$_2$ core-shell heterostructures as electrode materials for high-performance supercapacitors. We systematically probed structures and electrochemical properties of the heterostructures in which the CuO nanowires/nanotubes are designed as core, while the ultrathin MnO$_2$ nanosheets as shell. The complex heterostructures are found to show a high specific capacitance of 276 F g^{-1} at a current density of 0.6 A g^{-1}, much improved rate performance, and long-term cycling stability (92.1% of its original value after 1000 cycles), rendering such heterostructures promising for the application as high-performance supercapacitors.

Results

To determine the chemical composition and crystallite phase of the CuO@MnO$_2$ nanocomposites, we performed X-ray diffraction (XRD) analyses, as shown in Fig. 1, where XRD pattern of freshly prepared Cu nanowires is given as well (Supplementary Fig. S1). When the reaction time is 1 h, three sharp peaks occur at $2\theta =$ 43.5, 50.7, and 74.48°, which are correspondingly indexed as (111), (200) and (220) planes of face-centered cubic Cu (JCPDS card no. 03-1018). The diffraction peaks at $2\theta =$ 12.5°, 25.2°, 37° and 65.6° are, on the other hand, in line with standard XRD patterns of the birnessite-type manganese oxide crystal (JCPDS card no. 80-1098), which reveals the formation of MnO$_2$. When the reaction time is over 12 h, sharp peaks of Cu nanowires disappear. The weak peaks of CuO are detected instead, indicating that Cu nanowires are almost transformed to CuO. The samples prepared after over 24 h are found to be composed of mixed CuO and δ-MnO$_2$. We also find that the crystallinity is somewhat enhanced with the increase of hydrothermal reaction time.

Figure 2 presents SEM images of the samples prepared at different hydrothermal time. From Fig. 2a and b, one can see that surfaces of pristine Cu nanowires are rough and uniformly covered by close-packed MnO$_2$ nanoparticles. By contrast, the freshly prepared pristine Cu nanowires have a smoother surface (Supplementary Fig. S2). As the reaction time is over 12 h, surfaces of Cu nanowire are homogenously covered by ultrathin MnO$_2$ nanoflakes (Fig. 2c). On closer inspection, the individual hierarchical CuO@MnO$_2$ nanotube is determined to have a diameter of ~400 nm (Fig. 2d), much larger than the pristine Cu nanowires (90–150 nm). When the reaction time reaches 24 h, the CuO surfaces are covered by compact MnO$_2$ nanosheets (Fig. 2e and f), and the composites have a diameter of 700 nm, indicative of sufficient reaction of KMnO$_4$. However, when the reaction time is 48 h, there appear MnO$_2$ nanoflowers comprising nanosheets, which is due to the Ostwald ripening process[41,42], leading to self-assembly of small nanosheets to hierarchical nanostructures.

Figure 3 shows a typical TEM image of the hybrid CuO@MnO$_2$ nanocomposite prepared using 0.05 M KMnO$_4$ at 160°C for 24 h. The surfaces of CuO nanotubes are uniformly covered by thin
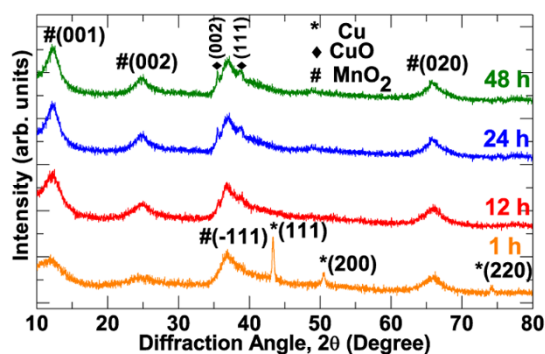
nanosheets (Fig. 3a and b), as confirmed in the scanning TEM (STEM) image (Supplementary Fig. S3b). Further analysis of the SAED pattern (Fig. 3b, inset) taken from the nanosheet edge reveals that the birnessite-type MnO$_2$ is polycrystalline[35,43]. From the HRTEM image (Fig. 3c), one can clearly see the lattice fringes with an interplanar spacing of 0.69 nm for the two curling nanosheets, which is identified as the typical interplanar spacing of the (001) plane of birnessite-type MnO$_2$. Energy-dispersive x-ray spectroscopy (EDS) analysis of individual composite reveals that there appears a distribution of O, K, Mn, and Cu across the core-shell structure (Fig. 3d and Supplementary Fig. S3). Interestingly, the K, Mn and O signals are detected in the entire structure, verifying that the core-shell is composed of hollow CuO nanotube supported MnO$_2$ nanosheets (Fig. 3d). This unique structure helps improve ionic transport and mechanical stability. We also prepared hybrid nanocomposites with 0.05 M KMnO$_4$ for 12 h, and identified that the CuO core is not completely hollow (Supplementary Fig. S4), indicating that reaction time is crucial to structural evolution of CuO interiors.

We therefore propose a possible growth mechanism for the hybrid CuO@MnO$_2$ core-shell structure (Fig. 4), which can be divided into three stages. Firstly, the MnO$_4^-$ nuclei are produced and adsorbed on surfaces of Cu nanowires, forming MnO$_2$ nuclei. With the increase of reaction time, the MnO$_2$ nuclei are aggregated and transformed to nanosheets. In the meanwhile, Cu nanowires are oxidized to CuO nanowires, followed by a transformation to CuO nanotubes. Finally, the MnO$_2$ nanosheets are compact and totally cover surfaces of CuO nanotubes, resulting in the formation of the hierarchical CuO nanotube@MnO$_2$ nanosheets nanocomposites. Such process is supported by the morphology evolution at different growth stages *via* tuning the reaction time (Fig. 4).

The formation of CuO nanotubes can also be explained by the mechanism similar to the Kirkendall effect at metal/oxide interface: the outward diffusion of metal ions is much faster than inward oxygen diffusion induced by the decomposition of KMnO$_4$ in hydrothermal reaction. The vacancies, which can diffuse to metals as a counterflow to the outward diffusion of metallic ions, can aggregate to generate voids. Such growth mechanism for the CuO nanotubes is in line with previous studies demonstrating that formation of oxide nanotube is through the Kirkendall-type diffusion process[44–46]. It is worthy of noting that the interconnected MnO$_2$ nanosheets and hollow CuO nanotubes give rise to a highly porous morphology, which can offer very high surface area and a large number of active sites for the adsorption of Na$^+$. These eventually lead to a high specific capacitance for CuO@MnO$_2$ composite. We therefore attribute the observed growth mechanism to a synergistic effect of Ostwald ripening process[47] which forms MnO$_2$ nanosheets and Kirkendall-type diffusion process[48] which is responsible for the formation of CuO nanotubes. Furthermore, we investigated the effect of concentration of KMnO$_4$ and reaction temperature on morphology of the composite and find that the relatively high concentration of KMnO$_4$ and high temperature favor the formation of the hierarchical CuO nanotube@MnO$_2$ nanosheets architectures (Supplementary Figs. S5 and S6).

Figure 5 shows XPS spectra of the composite, which are calibrated with reference to C 1s peak at 285 eV. The Mn 2p XPS spectrum exhibits two major peaks at binding energy of 654.75 and 642.95 eV with a spin-energy separation of 11.8 eV (Fig. 5a), in agreement with other reports[39,49,50]. As reported previously[51,52], the average oxidation state of Mn in manganese oxides can be determined by the energy separation of Mn 3s peaks. The CuO@MnO$_2$ hybrid structures exhibit a separated energy of 4.8 eV for the Mn 3s doublet (Fig. 5b), indicating that the Mn in the composite has a charge state of ~4.0. Figure 5c shows XPS of Cu 2p core level, from which the peaks at 954.2 and 934.45 eV are found to correspond to the Cu $_{2p1/2}$ and Cu $_{2p3/2}$, respectively, with a spin-orbit splitting of 19.75 eV. There are also two satellite peaks at 962.7 and 943.65 eV, which

Figure 1 | XRD patterns of CuO-MnO$_2$ nanocomposites obtained at different time.
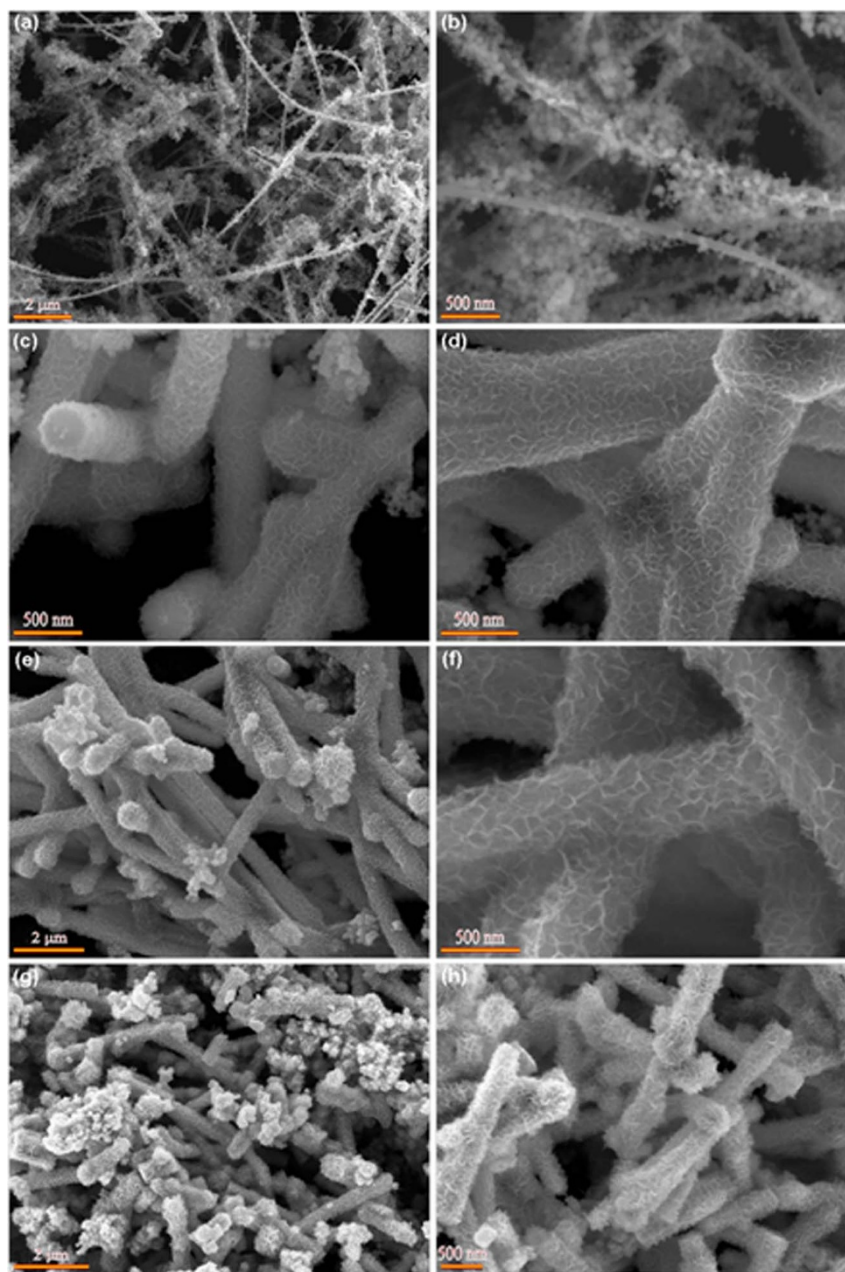
Figure 2 | SEM images of the samples obtained at different reaction time: a, b) 1 h; c, d) 12 h; e, f) 24 h; g, h) 48 h. Note that the samples were obtained with 0.05 M $KMnO_4$ solution at 160°C.

confirms the oxide in the sample as CuO[18,53,54]. These results also confirm the formation of $CuO@MnO_2$ composite, in good agreement with the XRD analysis. In addition, the fitted O 1 s spectrum is characterized by three bands (Fig. 5d): two at 532.3 and 531.3 eV, which is due to the absorption of oxygen and water molecules on the composite surface, and one at 530.4 eV, which corresponds to the O^{2-} band with Cu and Mn[39,55]. We also investigated XPS spectra of CuO/MnO_2 composite fabricated after 1 h, revealing the presence of the fitted Cu 2p spectrum. This also implies that Cu nanowires are, to some extent, oxidized even after reaction for 1 h (Supplementary Fig. S7).

To investigate surface property of the composite, we conducted FT-IR spectrum analysis. As shown in Fig. 6a, the broad band at ~3440 cm^{-1} indicates O–H stretching in water molecules, and the weak band at 1635 cm^{-1} may be due to bending vibration of O–H groups in the adsorbed water molecules. The peaks at ~1385 and 1117 cm^{-1} correspond to the coordination of Mn by the O–H. The

peak at 529 cm^{-1} is deemed as the main characteristic absorption band of birnessite, which corresponds to the Mn-O stretching modes of the octahedral layers in the birnessite[11]. Moreover, the weak band at 448 cm^{-1} can be due to the Cu-O stretching vibration. We therefore conclude that the products are mixed CuO and MnO_2, in good agreement with the XRD analysis.

Figure 6b shows thermal stability of the as-synthesized composite, where one can see the first weight loss (~11.5%) below 180°C, which is attributed to the removal of physically absorbed water and chemically bonded water. There are two endothermic DSC peaks at ~80°C and ~150°C, confirming the water evaporation. This feature can also be reflected in the TGA analysis. The second weight loss (~2%) in between 550 and 700°C can be attributed to the loss of oxygen in MnO_2 lattice, *i.e.* reduction of MnO_2 to Mn_2O_3[42,56,57], consistent with the sharp peak in the DSC curve.

To further investigate the surface property of the as-prepared nanocomposite, we measured the Brunnauer-Emmett-Teller (BET)
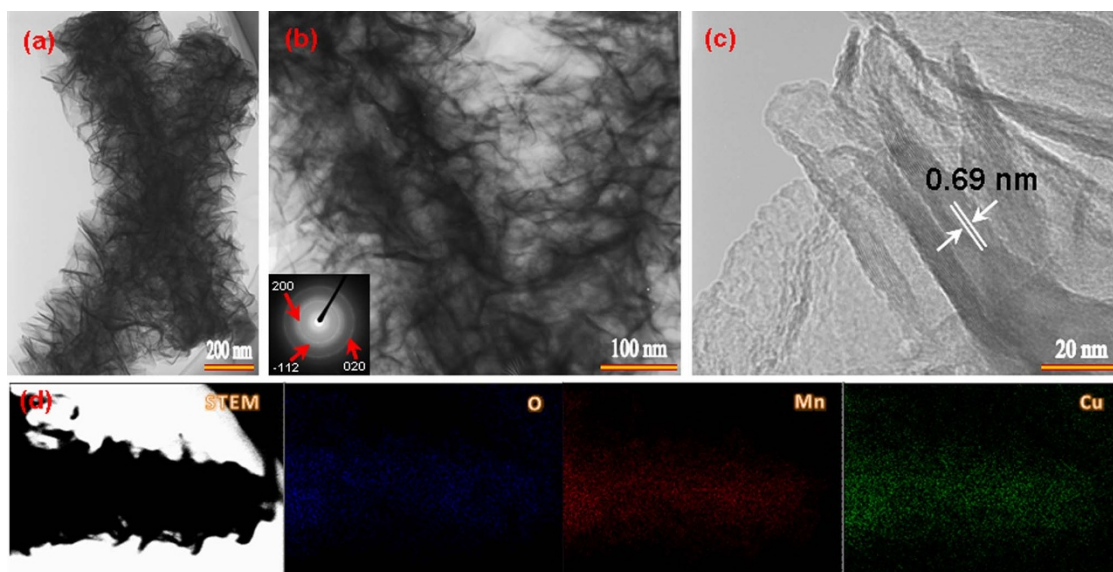
Figure 3 | (a) Low-magnification TEM images of the hierarchical CuO nanotube@MnO_2 nanosheets nanostructures. (b) Enlarged TEM image of the CuO@MnO_2 nanocomposite. The bottom-left inset shows the corresponding SAED pattern taken from the edge of nanosheet. (c) HRTEM image of the birnessite-type MnO_2 nanosheets. (d) STEM image and EDS mapping of the hierarchical CuO nanotube@MnO_2 nanosheets nanostructures. Note that the CuO nanotube@MnO_2 nanosheets composite was obtained with 0.05 M $KMnO_4$ at 160°C for 24 h.

and nitrogen adsorption-desorption, as shown in Fig. 7. The nanocomposite shows a typical type IV isotherm with hysteresis loop in a relative pressure (P/P_0) range of 0.7–1.0, implying the formation of slit-like pores by stacking the sheet-like MnO_2 building blocks. The BET surface area of the core-shell nanostructure is calculated to be 98 $m^2 g^{-1}$, and mean diameter of the pores is calculated to be 5 nm using Barett-Joyner-Halenda (BJH) model. The high BET specific surface area and mesoporous structure can enhance electron and ion transport, resulting in high electrochemical capacity for the nanocomposite. We also prepared nanocomposites with different reaction time and examined N_2 adsorption/desorption isotherms (Supplementary Fig. S8). We find that the nanocomposites obtained at 24 h show the largest BET surface area, which should broaden the contact area between the active materials and the electrolytes.

To evaluate the applications of the nanostructures as electrochemical capacitors, we fabricated electrodes in a three-electrode configuration (Fig. 8). Figure 8a presents the CV curves of CuO@MnO_2 electrodes in 1 M Na_2SO_4 aqueous electrolyte at various scan rates.

Although there are no distinct redox peaks, the shape of CV curve deviates from the ideal rectangle, implying that the electrode shows faradic pseudocapacitive nature. To further investigate electrochemical performances of the CuO@MnO_2 electrode, we perform galvanostatic charge-discharge curves at various current densities in an electrochemical window of $-0.2 \sim 0.8$ V (Fig. 8b). There appear a triangular symmetry and linear slopes, consolidating the good electrochemical performance. The specific capacitance is calculated to be 276 $F g^{-1}$ from the discharge curves at a current density of 0.6 $A g^{-1}$, which can be attributed to the highly porous structure and high specific surface area which facilitate ion transfer and thus enhance redox faradic reactions and surface adsorption of electrolyte cations. It is worthy of noting that the nanocomposite shows a higher specific capacitance compared to the MnO_2-based electrodes reported previously (Supplementary Table S1).

We further investigated the relationship between the specific capacitance and the current density (Supplementary Fig. S9) and found that the capacitance decreases with the increase of current density.
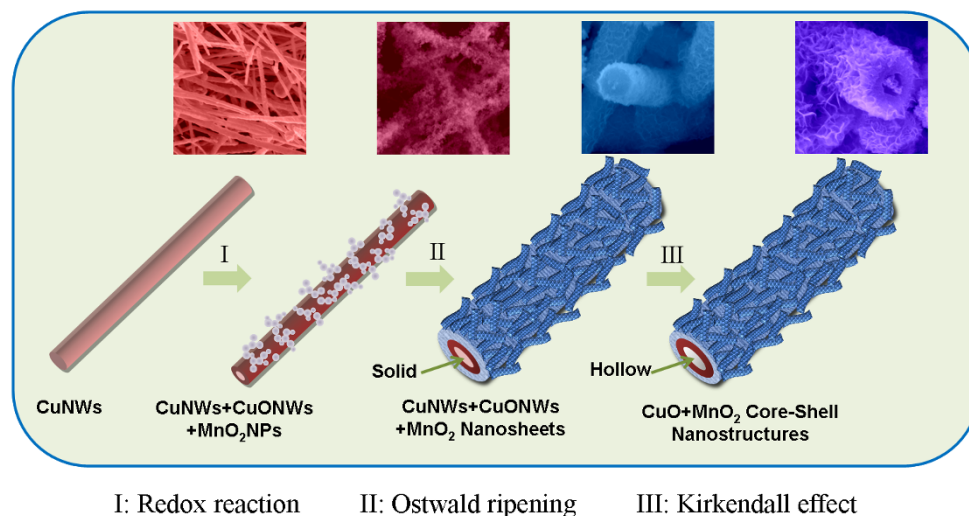

I: Redox reaction   II: Ostwald ripening   III: Kirkendall effect

Figure 4 | Schematic illustration of the growth mechanism of the CuO@MnO_2 core-shell nanostructures.
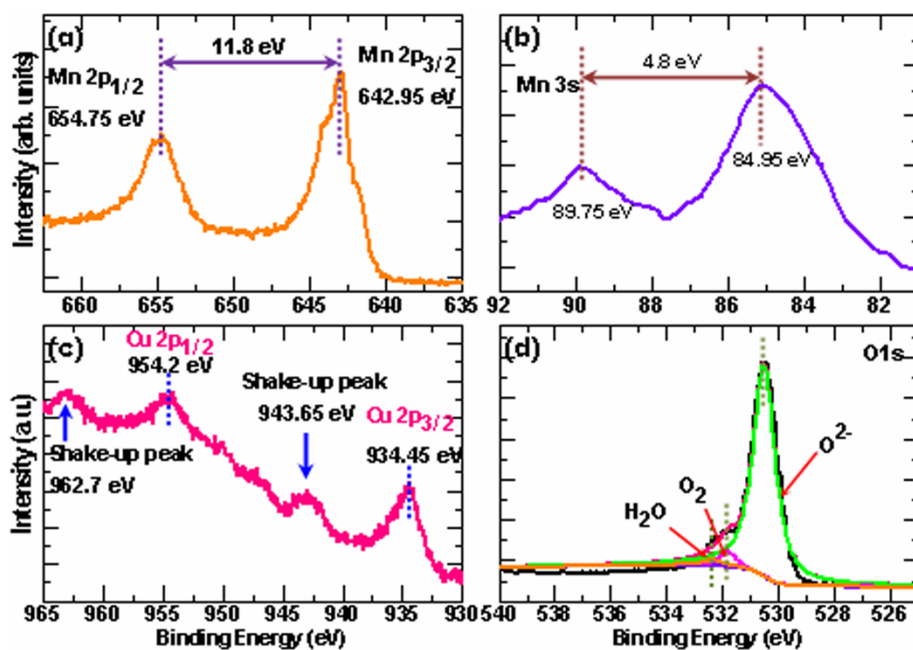
Figure 5 | XPS spectra of CuO nanotube@MnO₂ nanosheets core-shell structures obtained after 24 h of growth: a) Mn 2p spectrum; b) Mn 3s spectrum; c) Cu 2p spectrum; d) O 1s spectrum.

The CuO@MnO₂ electrode displays a moderate rate, *i.e.* 51% of its initial capacitance, when the current density increases from 0.6 to 10 A g⁻¹. The low capacitance at high current density can be attributed to the decrease in the utilization efficiency of the active material. We also measured the electrochemical properties of the nanostructures prepared at different reaction time (Supplementary Fig. S10). The nanocomposite prepared at 24 h shows the highest specific capacitance, nearly 1.5 times higher than the one prepared at 1 h, which indicates that morphology plays an important role in affecting electrochemical property.

The impedances of MnO₂-modified diatomite hierarchical electrode before and after 1000 cycles are also measured in the frequency range of 100 kHz–0.01 Hz at an open circuit potential by employing an AC voltage of 5 mV. As shown in Fig. 8c, the impedance spectra are composed of one semicircle at high frequency, followed by a linear shape at low frequency. The inset of Fig. 6c gives an equivalent circuit used to fit the impendence curve, consistent with the one employed for the working electrode of the supercapacitor. The electrochemical impendence spectral data are fitted by the internal resistance (Rs), the charge-transfer resistance (Rct), the Warburg impendence (Zw), the constant phase element (CPE) to address the double-layer capacitance, and the C_L to address the limited pseudo-faradic reaction[58]. Supplementary Table S2 lists the corresponding

equivalent circuit parameters fitted in the Nyquist plots for the CuO@MnO₂ electrodes before and after 1000 charge/discharge cycles. The internal resistances (Rs) of the MnO₂ electrodes change from 1.0 Ω to 1.4 Ω after 1000 cycles, manifesting a good conductivity of the electrolyte and the very low internal resistance of the electrode. The charge-transfer resistance (Rct), however, increases only a little from 15.6 to 17.2 Ω after 1000 cycles. Further investigation demonstrates that the hierarchical CuO@MnO₂ nanostructured electrode exhibits excellent electrochemical cycling stability.

Figure 8d shows the cycling stability of the as-prepared hierarchical CuO@MnO₂ nanostructures by conducting charge/discharge tests at a current density of 3 A g⁻¹ for 1000 cycles. The specific capacitance of the CuO@MnO₂ electrode maintains 92.1% of its initial value, indicating a good stability. The charge-discharge curves of the final 10 cycles are shown in inset of Fig. 8d, showing almost the same symmetric shape, which implies that the CuO@MnO₂ electrode does not undergo significant structural change during the charge/discharge processes. Further SEM imaging of the electrode uncovers that the hierarchically porous CuO@MnO₂ core-shell structure is maintained (Supplementary Fig. S11). Such unique nanostructure may solve the aggregation and volume expansion issue during long-term cycles, which benefit the structural stability of the CuO@MnO₂ electrode. This also demonstrates that this
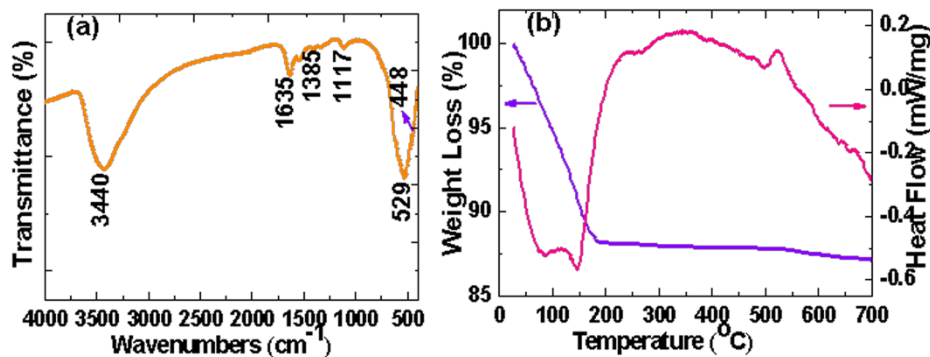

Figure 6 | FT-IR spectra (a) and TGA-DSC curves (b) of the as-prepared CuO-MnO₂ nanocomposite obtained with 0.05 M KMnO₄ at 160°C for 24 h.
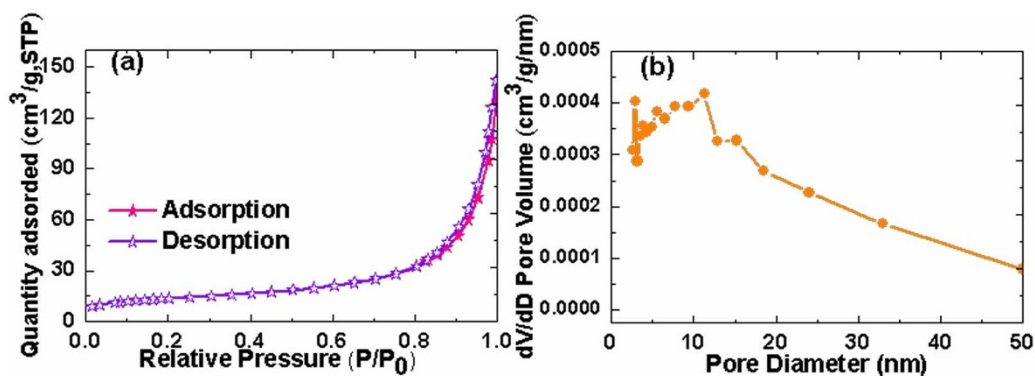
Figure 7 | N$_2$ adsorption-desorption isotherms (a) and corresponding pore size distribution (b) of the as-prepared CuO@MnO2 nanocomposite obtained with 0.05 M KMnO$_4$ at 160°C for 24 h.

nanocomposite can act as potential candidates for electrodes in supercapacitors.

Discussion

To test if the hybrid CuO@MnO$_2$ electrodes can be put into real applications, we fabricated asymmetric supercapacitors using the CuO@MnO$_2$ core-shell structures as positive electrode and the microwave exfoliated graphite oxide (MEGO) as negative electrode. The 1.0 M Na$_2$SO$_4$ aqueous electrolyte is applied. Figure 9a shows CV as a function of voltage for the CuO@MnO$_2$//MEGO asymmetric supercapacitor with an optimal mass ratio between two electrodes. The CuO@MnO$_2$ core-shell and MEGO materials have a weight of 0.8 and 1.0 mg, respectively. The supercapacitor shows an ideal capacitive behavior with quasi-rectangular CV curves at a scan rate of 50 mV s^{-1} even at the potential up to 2.0 V. The CV curves obtained under various scan rates at a voltage ranging from 0 to 1.8 V exhibit a rectangular-like shape (Fig. 9b), indicating that the device shows a fast charge/discharge behavior and a high rate ability.

Figure 9c shows galvanostatic charge/discharge curves, from which one can note that the potentials are nearly proportional to time, indicating a rapid I–V response and an ideal capacitive nature. The gravimetric capacitance (Ct) is calculated to be 49.2 F g^{-1} at current density of 0.25 A g^{-1}. We further assess a maximum gravimetric energy density of 22.1 Wh kg^{-1} and power density of 85.6 kW kg^{-1} (Fig. 9d) for our asymmetric supercapacitor, much higher than those of symmetrical supercapacitor or MnO$_2$-based asymmetric supercapacitor[42,59–63]. We further connected our prototype device to a red LED and successfully light the LED (inset in Fig. 9d). The LED is on for over 10 min after charged for 30 s at 1.8 V (Supplementary Movie S1). In addition, we tested the long-term cycle stability of this device at a current density of 3 Ag^{-1} for 10000 cycles, and found that the specific capacitance is increased gradually in the initial cycling test and turn steady. Although slight degradation tendency is observed in the final cycling test (Supplementary Fig. S12), the capacitance retains 101.5% of its initial value even after 10000 cycles, demonstrating a minimal damage and
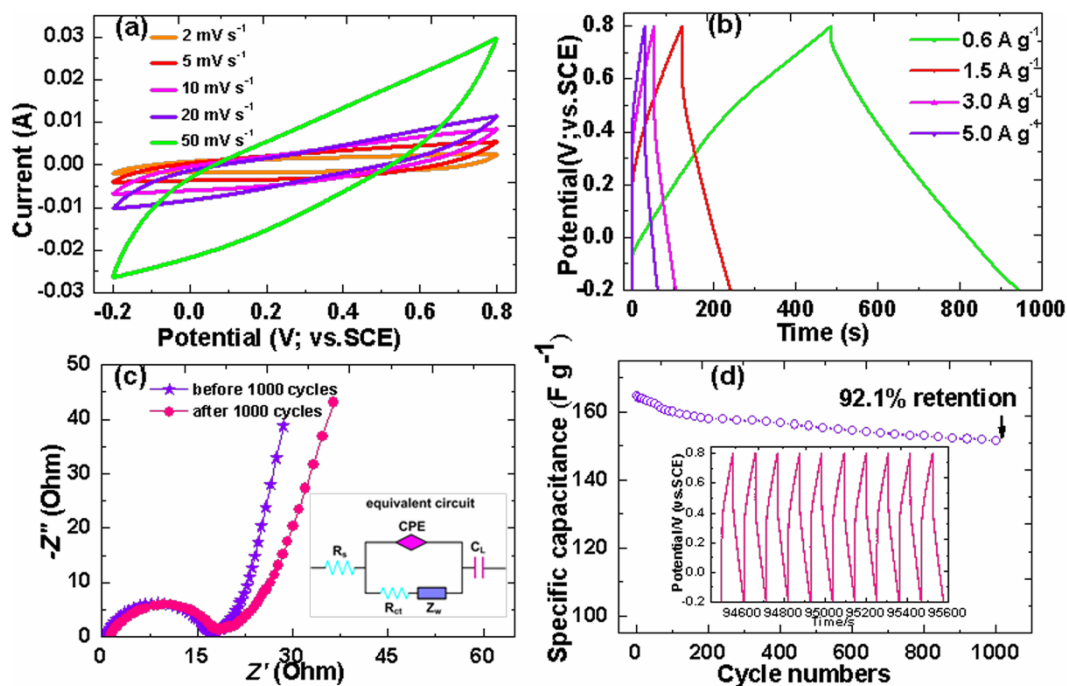

Figure 8 | (a) Cyclic voltammograms of CuO@MnO$_2$ nanocomposite in a 1 M Na$_2$SO$_4$ aqueous electrolyte; (b) charge-discharge curves of CuO@MnO$_2$ at different current densities; (c) the electrochemical impedance spectrum of the electrodes at open circuit potential in the frequency range from 0.01 Hz to 100 kHz. The inset shows the equivalent circuit; (d) cycling performance of the nanocomposite electrode at the current density of 5 A g^{-1}. The inset shows the charge-discharge curves of the last 10 cycles of the CuO@MnO$_2$ electrode.
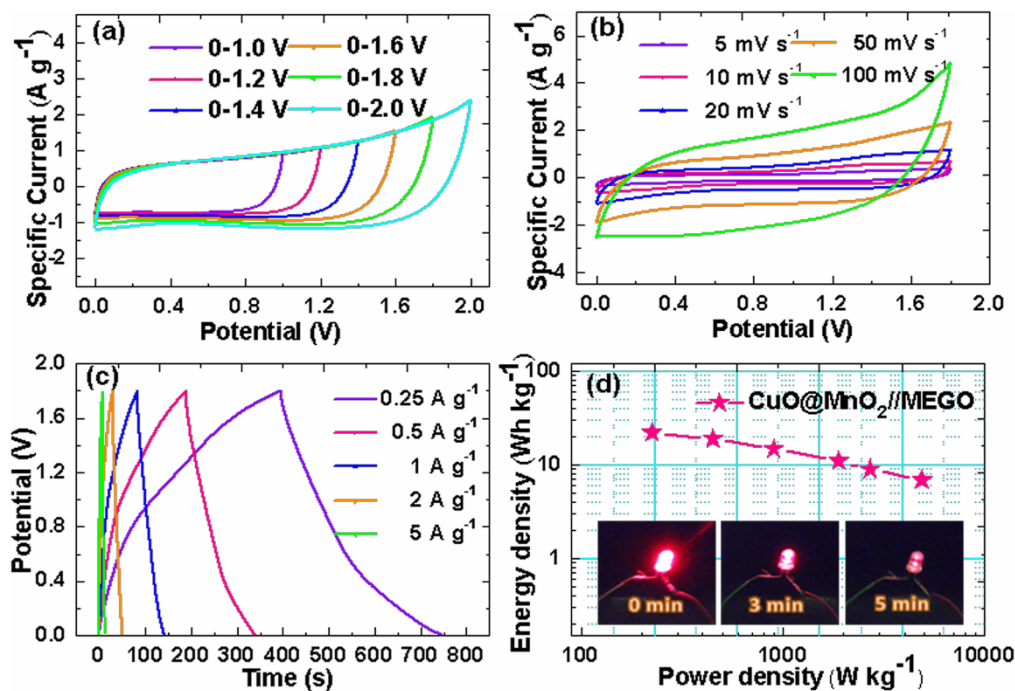
Figure 9 | (a) CV curves of CuO@MnO$_2$ core-shell nanostructures//MEGO asymmetric supercapacitor measured at different potential window at a scan rate of 50 mV s^{-1}. (b) CV curves of the asymmetric supercapacitor measured at different scan rates between 0 and 1.8 V. (c) Galvanostatic charge-discharge curves at different current densities. (d) Ragone plots of the asymmetric supercapacitor. The inset shows the digital image of a red-light-emitting diode (LED) lighted by the CuO@MnO$_2$//MEGO device.

disassembly of the electrode during redox reaction. These offer compelling evidence that the CuO@MnO$_2$/MEGO asymmetric supercapacitor device holds substantial promise for practical applications.

To conclude, we have developed a facile and cost-effective method to synthesize a hierarchical core-shell CuO@MnO$_2$ nanocomposite and demonstrate its application as efficient electrodes for high-performance supercapacitors. By taking advantage of the hybridization of CuO and MnO$_2$, we demonstrate that the electrode fabricated by the as-prepared CuO@MnO$_2$ nanocomposite shows a specific capacitance of 276 F g^{-1}. We also fabricate asymmetric supercapacitors in the form of fully packaged cells, and demonstrate that the device can be reversibly charged and discharged at an operation voltage of 1.8 V in 1.0 M Na$_2$SO$_4$ aqueous electrolyte. Moreover, the device delivers an energy density of 22.1 Wh kg^{-1}, a maximum power density of 85.6 kW kg^{-1}, and a long-term cycling stability which retains 101.5% of its initial capacitance even after 10000 cycles. The new CuO@MnO$_2$ coaxial nanostructure with remarkably enhanced capacitive behaviors adds instantly a novel practical route for the elegant design of electrodes for high-performance supercapacitors.

Methods

Synthesis of Cu nanowires. All chemical regents were of analytical purity and used with no further purification, including the copper nitrate (Cu(NO$_3$)$_2$•2.5H$_2$O), sodium hydrate (NaOH), ethylenediamine (EDA, C$_2$H$_8$N$_2$, 99%), hydrazine monohydrate (N$_2$H$_4$•H$_2$O, 98%), potassium permanganate (KMnO$_4$), and ethanol (C$_2$H$_5$OH). The copper nanowires were prepared by reducing copper (II) nitrate with hydrazine in the alkaline medium[46,64]. An aqueous solution of Cu(NO$_3$)$_2$•2.5H$_2$O (1 mL, 0.1 M) was mixed with NaOH (20 mL,15 M). The ethylenediamine (EDA, 150 μL) and hydrazine (35 μL, 35 wt.%) were then added sequentially. The mixture was next stirred utterly. The reactor was placed in water bath at 65°C for 1 h. Finally, the resulting products were filtered, washed with distilled water and ethanol several times, and dried at 60°C in vacuum oven for 6 h.

Fabrication of the CuO nanotube@MnO$_2$ nanosheet core-shell nanostructures. The CuO@MnO$_2$ nanocomposites were prepared without any surfactant using a facile and scaleable method. First, the Cu nanowires (10 mg) were dispersed in KMnO$_4$ solution (30 mL, 0.01–0.1 M) to form a homogeneous precursor. The mixture was then put into a Teflon-lined stainless steel autoclave which was

subsequently maintained at 160°C for 24 h. Finally, the sample was removed, washed with distilled water and ethanol, and dried at 60°C.

Material characterization. The crystallography and chemical composition of the as-prepared products were investigated by powder X-ray diffraction (XRD, D/max 1200, Cu K) and Fourier transform infrared spectroscopy (FTIR, Nicolet 5DXC). The morphologies of the CuO@MnO$_2$ composites were observed with focused ion beam (Zeiss Auriga FIB/SEM). Microstructures were characterized by transmission electron microscopy (TEM), high-resolution TEM, and energy-dispersive x-ray spectroscopy (EDS) using JEOL JEM-2010F electron microscope operated at 200 kV. The nitrogen adsorption-desorption isotherms were measured at 77 K using micrometritics ASAP 2020 sorptometer. Specific surface area was determined with Brunauer-Emmett-Teller (BET) equation, and the distribution of pore size was calculated from the adsorption curve by the Barrett–Joyner–Halenda (BJH) method.

Electrochemical measurements. A three-electrode system was applied to measure the response of CuO@MnO$_2$ nanostructures as working electrode. The Na$_2$SO$_4$ aqueous solution (1 M), platinum plate, and saturated calomel electrode (SCE) were employed as electrolyte, counter and reference electrode, respectively. The working electrode was prepared by mixing 70 wt% active material (CuO@MnO$_2$), 20 wt% acetylene black and 10 wt% polyvinylidene fluoride (PVDF) in N-methyl-2-pyrrolidone (NMP). The slurry was spread onto a foam nickel current collector (1 × 1 cm^2). The electrode was heated at 120°C for 12 h to evaporate solvent and then uniaxially pressed under 10 MPa. The electrode contained 2–3 mg active CuO@MnO$_2$ material.

The supercapacitor performance was measured using a two-electrode system that is composed of two slices of electrode materials with identical shape, a filter paper as separator, and two nickel foils as current collectors. In the two-electrode system, the CuO@MnO$_2$ nanostructures acted as a positive electrode. The negative electrode was prepared by putting the mixed paste of activated microwave exfoliated graphite oxide (MEGO) with 20 wt% acetylene black and 10 wt% polyvinylidene fluoride (PVDF) in N-methyl-2-pyrrolidone (NMP) onto the uniform sheets. The two electrodes were assembled together by soaking the filter paper in Na$_2$SO$_4$ solution in prior to be connected to potentiostat. The performances for both three-electrode and two-electrode configurations were measured with CHI 660E electrochemical station. The cyclic voltammetry (CV) and galvanostatic charge-discharge technique were used to probe electrochemical performance of the electrodes. The operating current density was calculated based on the mass of active materials, that is, the mass of CuO@MnO$_2$ for the three-electrode system and the total weight of CuO@MnO$_2$ and MEGO for the two-electrode system. Electrochemical impedance spectroscopy (EIS) was measured in the frequency range from 100 kHz to 0.01 Hz with perturbation amplitude of 5 mV.

1. Miller, J. R. & Simon, P. Materials science - Electrochemical capacitors for energy management. *Science* **321**, 651–652 (2008).

2. Simon, P. & Gogotsi, Y. Materials for electrochemical capacitors. *Nat. Mater.* **7**, 845–854 (2008).

3. Wei, D. *et al.* A Nanostructured electrochromic supercapacitor. *Nano Lett.* **12**, 1857–1862 (2012).

4. Wang, G., Zhang, L. & Zhang, J. A review of electrode materials for electrochemical supercapacitors. *Chem. Soc. Rev.* **41**, 797–828 (2012).

5. Chen, W. *et al.* High-performance nanostructured supercapacitors on a sponge. *Nano Lett.* **11**, 5165–5172 (2011).

6. Chaikittisilp, W. *et al.* Nanoporous carbons through direct carbonization of a zeolitic imidazolate framework for supercapacitor electrodes. *Chem. Commun. (Camb)* **48**, 7259–7261 (2012).

7. Itoi, H., Nishihara, H., Kogure, T. & Kyotani, T. Three-dimensionally arrayed and mutually connected 1.2-nm nanopores for high-performance electric double layer capacitor. *J. Am. Chem. Soc.* **133**, 1165–1167 (2011).

8. Rakhi, R. B., Chen, W., Cha, D. & Alshareef, H. N. Substrate dependent self-organization of mesoporous cobalt oxide nanowires with remarkable pseudocapacitance. *Nano Lett.* **12**, 2559–2567 (2012).

9. He, X. *et al.* Synthesis of mesoporous carbons for supercapacitors from coal tar pitch by coupling microwave-assisted KOH activation with a MgO template. *Carbon* **50**, 4911–4921 (2012).

10. Chen, K., Noh, Y. D., Li, K., Komarneni, S. & Xue, D. Microwave-hydrothermal crystallization of polymorphic MnO_2 for electrochemical energy storage. *J. Phys. Chem. C* **117**, 10770–10779 (2013).

11. Zhang, Y. X., Huang, M., Li, F., Wang, X. L. & Wen, Z. Q. One-pot synthesis of hierarchical MnO_2-modified diatomites for electrochemical capacitor electrodes. *J. Power Sources* **246**, 449–456 (2014).

12. Yuan, C. *et al.* Growth of ultrathin mesoporous Co_3O_4 nanosheet arrays on Ni foam for high-performance electrochemical capacitors. *Energy Environ. Sci.* **5**, 7883–7887 (2012).

13. Shim, H.-W. *et al.* Scalable one-pot bacteria-templating synthesis route toward hierarchical, porous-Co_3O_4 superstructures for supercapacitor electrodes. *Sci. Rep.* **3**, 2325 (2013).

14. Zhang, G., Yu, L., Hoster, H. E. & Lou, X. W. Synthesis of one-dimensional hierarchical NiO hollow nanostructures with enhanced supercapacitive performance. *Nanoscale* **5**, 877–881 (2013).

15. Ji, J. *et al.* Nanoporous $Ni(OH)_2$ thin film on 3D ultrathin-graphite foam for asymmetric supercapacitor. *ACS Nano* **7**, 6237–6243 (2013).

16. Qu, Q. T., Liu, L. L., Wu, Y. P. & Holze, R. Electrochemical behavior of $V_2O_5 \cdot 0.6H_2O$ nanoribbons in neutral aqueous electrolyte solution. *Electrochim. Acta* **96**, 8–12 (2013).

17. Qu, Q., Zhu, Y., Gao, X. & Wu, Y. Core-shell structure of polypyrrole grown on V_2O_5 nanoribbon as high performance anode material for supercapacitors. *Adv. Energy Mater.* **2**, 950–955 (2012).

18. Dubal, D. P. *et al.* Surfactant-assisted morphological tuning of hierarchical CuO thin films for electrochemical supercapacitors. *Dalton Trans.* **42**, 6459–6467 (2013).

19. Zhang, Y. X. *et al.* Facile Synthesis of mesoporous CuO manoribbons for electrochemical capacitors applications. *Int. J. Electrochem. Sci.* **8**, 1366–1381 (2013).

20. Li, Y. *et al.* Nanostructured CuO directly grown on copper foam and their supercapacitance performance. *Electrochim. Acta* **85**, 393–398 (2012).

21. Wang, F. *et al.* Electrode materials for aqueous asymmetric supercapacitors. *RSC Adv.* **3**, 13059–13084 (2013).

22. Zhang, X., Sun, X., Zhang, H., Zhang, D. & Ma, Y. Microwave-assisted reflux rapid synthesis of MnO_2 nanostructures and their application in supercapacitors. *Electrochim. Acta* **87**, 637–644 (2013).

23. Guo, C. X., Wang, M., Chen, T., Lou, X. W. & Li, C. M. A Hierarchically nanostructured composite of MnO_2/conjugated polymer/graphene for high-performance lithium ion batteries. *Adv. Energy Mater.* **1**, 736–741 (2011).

24. Zhang, Y. *et al.* Crystallization design of MnO_2 towards better supercapacitance. *CrystEngComm* **14**, 5892–5897 (2012).

25. Lei, Z., Zhang, J. & Zhao, X. S. Ultrathin MnO_2 nanofibers grown on graphitic carbon spheres as high-performance asymmetric supercapacitor electrodes. *J. Mater. Chem.* **22**, 153–160 (2012).

26. Lee, S. W., Gallant, B. M., Byon, H. R., Hammond, P. T. & Shao-Horn, Y. Nanostructured carbon-based electrodes: bridging the gap between thin-film lithium-ion batteries and electrochemical capacitors. *Energy Environ. Sci.* **4**, 1972–1985 (2011).

27. Hu, L. *et al.* Stretchable, porous, and conductive energy textiles. *Nano Lett.* **10**, 708–714 (2010).

28. Chen, P.-C., Shen, G., Shi, Y., Chen, H. & Zhou, C. Preparation and characterization of flexible asymmetric supercapacitors based on transition-metal-oxide nanowire/single-walled carbon nanotube hybrid thin-film electrodes. *ACS Nano* **4**, 4403–4411 (2010).

29. Fischer, A. E., Pettigrew, K. A., Rolison, D. R., Stroud, R. M. & Long, J. W. Incorporation of homogeneous, nanoscale MnO_2 within ultraporous carbon structures via self-limiting electroless deposition: Implications for electrochemical capacitors. *Nano Lett.* **7**, 281–286 (2007).

30. Sumboja, A., Foo, C. Y., Wang, X. & Lee, P. S. Large areal mass, flexible and free-standing reduced graphene oxide/manganese dioxide paper for asymmetric supercapacitor device. *Adv. Mater.* **25**, 2809–2815 (2013).

31. Tao, J. *et al.* Solid-state high performance flexible supercapacitors based on polypyrrole-MnO_2-carbon fiber hybrid structure. *Sci. Rep.* **3**, 2286 (2013).

32. Deng, L. *et al.* Preparation and capacitance of graphene/multiwall carbon nanotubes/MnO_2 hybrid material for high-performance asymmetrical electrochemical capacitor. *Electrochim. Acta* **89**, 191–198 (2013).

33. Yu, L., Zhang, G., Yuan, C. & Lou, X. W. Hierarchical $NiCo_2O_4$@MnO_2 core-shell heterostructured nanowire arrays on Ni foam as high-performance supercapacitor electrodes *Chem. Commun.* **49**, 137–139 (2013).

34. Wei, W., Cui, X., Chen, W. & Ivey, D. G. Manganese oxide-based materials as electrochemical supercapacitor electrodes. *Chem. Soc. Rev.* **40**, 1697–1721 (2011).

35. Liu, J. *et al.* Co_3O_4 nanowire@MnO_2 ultrathin nanosheet core/shell arrays: a new class of high-performance pseudocapacitive materials *Adv. Mater.* **23**, 2076–2081 (2011).

36. Sarkar, D., Khan, G. G., Singh, A. K. & Mandal, K. High-performance pseudocapacitor electrodes based on α-Fe_2O_3/MnO_2 core–shell nanowire heterostructure arrays. *J. Phys. Chem. C* **117**, 15523–15531 (2013).

37. Yang, P. *et al.* Hydrogenated ZnO core-shell nanocables for flexible supercapacitors and self-powered systems. *ACS Nano* **7**, 2617–2626 (2013).

38. Lu, X. *et al.* H-TiO_2@MnO_2//H-TiO_2@C core-shell nanowires for high performance and flexible asymmetric supercapacitors *Adv. Mater.* **25**, 267–272 (2013).

39. Luo, Y. *et al.* Hierarchical TiO_2 nanobelts@MnO_2 ultrathin nanoflakes core-shell array electrode materials for supercapacitors *RSC Adv.* **3**, 14413–14422 (2013).

40. Xia, H. *et al.* Hierarchically structured Co_3O_4@Pt@MnO_2 nanowire arrays for high-performance supercapacitors *Sci. Rep.* **3**, 2978 (2013).

41. Li, Y. *et al.* Facile controlled synthesis and growth mechanisms of flower-like and tubular MnO_2 nanostructures by microwave-assisted hydrothermal method. *J. Colloid Inter. Sci.* **369**, 123–128 (2012).

42. Zhang, X. *et al.* Rapid hydrothermal synthesis of hierarchical nanostructures assembled from ultrathin birnessite-type MnO_2 nanosheets for supercapacitor applications. *Electrochim. Acta* **89**, 523–529 (2013).

43. Zhou, J. *et al.* Novel synthesis of birnessite-type MnO_2 nanostructure for water treatment and electrochemical capacitor. *Ind. Eng. Chem. Res.* **52**, 9586–9593 (2013).

44. Nakamura, R., Matsubayashi, G., Tsuchiya, H., Fujimoto, S. & Nakajima, H. Formation of oxide nanotubes via oxidation of Fe, Cu and Ni nanowires and their structural stability: Difference in formation and shrinkage behavior of interior pores. *Acta Mater.* **57**, 5046–5052 (2009).

45. Wang, Q., Chen, G., Wang, L., Zhou, C. & Xu, S. Self-sacrificed template method for the synthesis of ZnO-tubular nanostructures:reaction kinetics and pathways. *J. Cryst. Growth* **311**, 3978–3983 (2009).

46. Chang, Y., Lye, M. L. & Zeng, H. C. Large-scale synthesis of high-quality ultralong copper nanowires. *Langmuir* **21**, 3746–3748 (2005).

47. Zeng, H. C. Ostwald ripening: A synthetic approach for hollow nanomaterials. *Curr. Nanosci.* **3**, 177–181 (2007).

48. Wang, W., Dahl, M. & Yin, Y. Hollow nanocrystals through the nanoscale kirkendall effect. *Chem. Mater.* **25**, 1179–1189 (2013).

49. Zhao, Y., Jiang, P. & Xie, S.-S. ZnO-template-mediated synthesis of three-dimensional coral-like MnO_2 nanostructure for supercapacitors. *J. Power Sources* **239**, 393–398 (2013).

50. Reddy, A. L. M., Shaijumon, M. M., Gowda, S. R. & Ajayan, P. M. Coaxial MnO_2/ carbon nanotube array electrodes for high-performance lithium batteries. *Nano Lett.* **9**, 1002–1006 (2009).

51. Zhi, M., Manivannan, A., Meng, F. & Wu, N. Highly conductive electrospun carbon nanofiber/MnO_2 coaxial nano-cables for high energy and power density supercapacitors. *J. Power Sources* **208**, 345–353 (2012).

52. Sun, M. *et al.* Controlled synthesis of nanostructured manganese oxide: crystalline evolution and catalytic activities. *CrystEngComm* **15**, 7010–7018 (2013).

53. Ranjith Kumar, D., Manoj, D. & Santhanalakshmi, J. Optimization of site specific adsorption of oleylamine capped CuO nanoparticles on MWCNTs for electrochemical determination of guanosine. *Sensor. Actuat. B: Chem.* **188**, 603–612 (2013).

54. Yin, M. *et al.* Copper oxide nanocrystals. *J. Am. Chem. Soc.* **127**, 9506–9511 (2005).

55. Du, G. *et al.* Co_3O_4 nanoparticle-modified MnO_2 nanotube bifunctional oxygen cathode catalysts for rechargeable zinc-air batteries. *Nanoscale* **5**, 4657–4661 (2013).

56. Munaiah, Y., Raj, B. G. S., Kumar, T. P. & Ragupathy, P. Facile synthesis of hollow sphere amorphous MnO_2: the formation mechanism, morphology and effect of a bivalent cation-containing electrolyte on its supercapacitive behavior. *J. Mater. Chem. A* **1**, 4300–4306 (2013).

57. Dong, M. *et al.* Self-assembled spongy-like MnO_2 electrode materials for supercapacitors. *Physica E* **45**, 103–108 (2012).

58. Fang, D.-L., Chen, Z.-D., Liu, X., Wu, Z.-F. & Zheng, C.-H. Homogeneous growth of nano-sized beta-$Ni(OH)_2$ on reduced graphene oxide for high-performance supercapacitors. *Electrochim. Acta* **81**, 321–329 (2012).

59. Qu, Q. T. *et al.* A new cheap asymmetric aqueous supercapacitor: Activated carbon//$NaMnO_2$. *J. Power Sources* **194**, 1222–1225 (2009).

60. He, Y. *et al.* Freestanding three-dimensional graphene/MnO_2 composite networks as ultra light and flexible supercapacitor electrodes. *ACS Nano* **7**, 174–182 (2013).

61. Cottineau, T., Toupin, M., Delahaye, T., Brousse, T. & Belanger, D. Nanostructured transition metal oxides for aqueous hybrid electrochemical supercapacitors. *Appl. Phys. A-Mater.* **82**, 599–606 (2006).

62. Khomenko, V., Raymundo-Pinero, E., Frackowiak, E. & Beguin, F. High-voltage asymmetric supercapacitors operating in aqueous electrolyte. *Appl. Phys. A-Mater.* **82**, 567–573 (2006).

63. Cheng, Q. *et al.* Graphene and nanostructured MnO_2 composite electrodes for supercapacitors. *Carbon* **49**, 2917–2925 (2011).

64. Zhang, Y., Huang, M., Li, F., Zhao, H. & Wen, Z. Decoration of Cu nanowires with chemically modified TiO_2 nanoparticles for their improved photocatalytic performance. *J. Mater. Sci.* **48**, 6728–6736 (2013).

Acknowledgments

Author contributions

Y.X.Z., Z.C.W. and Q.L. conceived and designed the experiments. M.H. prepared materials and electrodes, and wrote the manuscript. F.L. conducted electrochemical measurements. Z.Y.W., A.M. and N.H. assisted the observations and measurements. Y.X.Z., Z.C.W. and Q.L. discussed the results and directed the entire study. All authors read and commented on the paper.

Additional information

How to cite this article: Huang, M. *et al.* Merging of Kirkendall Growth and Ostwald Ripening: CuO@MnO2 Core-shell Architectures for Asymmetric Supercapacitors. *Sci. Rep.* **4**, 4518; DOI:10.1038/srep04518 (2014).